

# Grid Edge Intelligence-Assisted Model Predictive Framework for Black Start of Distribution Systems With Inverter-Based Resources

Junyuan Zheng<sup>1</sup>, Graduate Student Member, IEEE, Salish Maharjan<sup>1</sup>, Senior Member, IEEE, and Zhaoyu Wang<sup>1</sup>, Fellow, IEEE

**Abstract**—The growing proliferation of distributed energy resources (DERs) is significantly enhancing the resilience and reliability of distribution systems. However, a substantial portion of behind-the-meter (BTM) DERs is often overlooked during black start (BS) and restoration processes. Existing BS strategies that utilize grid-forming (GFM) battery energy storage systems (BESS) frequently ignore critical frequency security and synchronization constraints. To address these limitations, this paper proposes a predictive framework for bottom-up BS that leverages the flexibility of BTM DERs through Grid Edge Intelligence (GEI). A predictive model is developed for GEI to estimate multi-period flexibility ranges and track dispatch signals from the utility. A frequency-constrained BS strategy is then introduced, explicitly incorporating constraints on frequency nadir, rate-of-change-of-frequency (RoCoF), and quasi-steady-state (QSS) frequency. The framework also includes synchronizing switches to enable faster and more secure load restoration. Notably, it requires GEI devices to communicate only their flexibility ranges and the utility to send dispatch signals—without exchanging detailed asset information. The proposed framework is validated using a modified IEEE 123-bus test system, and the impact of GEI is demonstrated by comparing results across various GEI penetration scenarios.

**Index Terms**—Distributed energy resources, model predictive control, grid-forming, grid edge intelligence, frequency security, synchronization.

## I. INTRODUCTION

THE Distribution System (DS) is reportedly vulnerable to high-impact, low-probability events such as hurricanes, tornadoes, and ice storms. These events often trigger widespread blackouts that adversely impact economic and social security. Therefore, rapid load restoration following a blackout, known as black start (BS), is critical to the resilience and reliability of the power system. More importantly, BS supported by Distributed Energy Resources (DERs) and Grid Edge Intelligence (GEI) is expected to replace conventional BS resources such as diesel generators.

Black start and load-restoration strategies can generally be classified into two categories: (a) top-down and (b) bottom-up strategies [1], [2]. The top-down approach relies on the transmission grid (TG) for restoration and is applicable when the blackout is localized within the DS. In the event of a large-scale power outage, typically caused by extreme weather, the bottom-up strategy helps restore the load even in the absence of an upstream transmission system. Traditionally, bottom-up strategies have been supported by BS units such as diesel generators [3]. Utilities maintain diesel generators as backup units for emergency situations due to their high operating costs [4]. However, BESS with grid-forming (GFM) inverters are now regarded as alternative BS units. The adoption of BESS is growing due to reduced production costs [5] and, unlike diesel units, they can be operated during both normal and emergency periods. Additionally, the increasing prevalence of DERs, including wind turbines, Photovoltaic (PV) systems, and small-scale storage at customer premises, has provided ample non-BS resources that can be leveraged with BESS for bottom-up black start. These resources offer several advantages over diesel generators, including high self-starting speed, lower operating costs, and fast dynamic response [6].

Currently, the DERs-aided black start has emerged as an effective and economical solution for providing restoration services following a blackout [7]. In [8], the coordination of multiple DERs is utilized to pick up the critical load during power outages. With advancements in GFM, GFM-based DERs can independently regulate system frequency and voltage, thereby enhancing their black start capability [9], [10]. So far, DER-aided black start strategies can be broadly classified into two categories: optimization-based [12]- [14] and machine learning-based strategies [15], [16]. The former approach focuses on reformulating the load restoration problem as an optimization problem to determine the final network topology, while the latter employs machine learning to train models for making load restoration decisions.

However, most of the literature in this vein concentrates on steady-state operation conditions, while less attention has been paid to dynamic frequency security constraints during the restoration process. In practice, the frequency of a microgrid tends to decline as loads are picked up. Therefore, incorporating frequency security constraints into the restoration process is essential to ensure stable and reliable BS. In [17], the

AQ:1 Received 21 April 2025; revised 23 October 2025; accepted 27 December 2025. This work was supported in part by the National Science Foundation under Grant ECCS 2042314 and in part by the Power System Engineering and Research Center under Grant PSERC S-110. Paper no. TSG-00743-2025. (Corresponding author: Zhaoyu Wang.)

The authors are with the Department of Electrical and Computer Engineering, Iowa State University, Ames, IA 50010 USA (e-mail: zhengjy@iastate.edu; salish@iastate.edu; wzy@iastate.edu).

Digital Object Identifier 10.1109/TSG.2026.3652515

TABLE I  
LITERATURE COMPARISON

Reference	BTM DER	GfMI	Frequency Security	Dynamic MG	MPC
[1]	✗	✗	✗	✓	✓
[2][15][16]	✗	✓	✗	✓	✗
[3][4][5][8][14]	✗	✗	✗	✓	✗
[6][17]	✗	✗	✓	✗	✗
[7][11]	✓	✗	✗	✗	✓
[9][18][19]	✗	✓	✓	✗	✗
[10]	✗	✓	✓	✓	✗
[21][22]	✓	✗	✗	✗	✗
<b>Proposed</b>	✓	✓	✓	✓	✓

frequency response of distributed generators is derived and incorporated into load restoration. Nevertheless, the dynamic frequency behavior of the distributed generators still requires detailed simulation for a more accurate analysis. In [18], the frequency nadir constraint is considered during the restoration of multiple microgrids, enabling the estimation of the frequency nadir limit without simulating the complex dynamic model of BS generators. While considering only the frequency nadir constraint is insufficient, the system frequency must also satisfy the rate of change of frequency (RoCoF) and quasi-steady-state (QSS) frequency constraints during load restoration. In [19], dynamic frequency constraints are taken into account in the load restoration process, which incorporates DERs based on GFM and grid-following (GFL) inverters. Nonetheless, this approach relies on simulations, which can be computationally intensive for large-scale restoration planning problems. Hence, there is an urgent need to model dynamic frequency constraints that are both accurate and practical for load restoration. Additionally, since the microgrid frequency tends to deviate when loads are picked up, it is essential to determine whether the frequency of a formed islanded MG is synchronized with other islanded MGs and with the TG. The aforementioned studies overlook synchronization both among islanded MGs and between islanded MGs and the TG, which can result in the formation of multiple islanded MGs. Meanwhile, BESS-based BS units cannot ensure long-term operation of restored MGs, given their finite energy capacity. Therefore, synchronization should be integrated into the blackstart process for stable load restoration.

Moreover, current bottom-up black start strategies primarily rely on utility-controlled DERs for load restoration. However, behind-the-meter (BTM) DERs, which are owned by individual customers, cannot be directly controlled by the utility due to privacy protection and ownership limitations. As a result, the potential contribution of the substantial number of BTM DERs during black start is often neglected. For instance, in [20], individual residential loads are directly modeled as cold loads, without accounting for the availability of BTM DERs. With the advancement of grid-side intelligence, the flexibility of behind-the-meter DERs can be estimated and incorporated into load restoration planning, accelerating the restoration process. Hence, the utilization of behind-the-meter DERs needs further

investigation. To distinguish this paper from existing relevant works, a comparative summary is presented in Table. I.

This paper proposes a model predictive framework for a bottom-up BS strategy that coordinates with multiple GEI systems to enhance load restoration. In this approach, each GEI communicates its multi-period flexibility range to the utility responsible for black start. In return, the utility provides a dispatch signal that the GEI devices track. This coordination mechanism ensures data privacy by eliminating the need for either the GEI devices or the utility to share proprietary information about their assets, network configurations, or control strategies. The utility's black start function is designed to restore the DS using multiple GFM BESS, which establish multiple microgrids. Each microgrid then coordinates with GEI to create cranking paths that bring GFL resources online. These resources help sustain the energized sections and prepare the system to restore the remaining unenergized sections. The paper also models the response of grid-forming inverters to load pickup, analyzing key frequency characteristics such as frequency nadir, rate of change of frequency (RoCoF), and quasi-steady-state (QSS) frequency. Additionally, it incorporates the role of synchronizing switches, which enable the integration of smaller microgrids into larger ones. This integration enhances the overall power and energy capacity, facilitating faster load restoration.

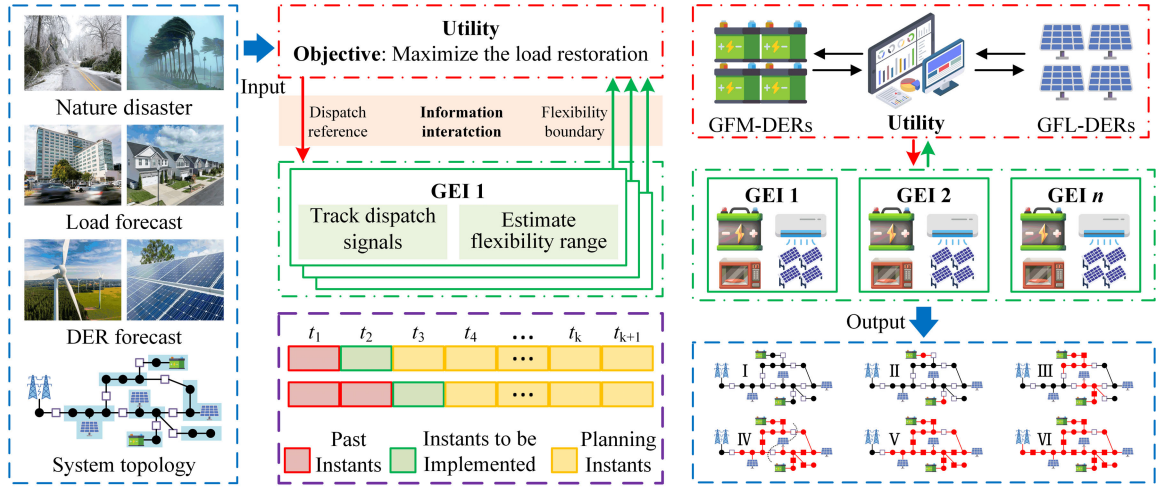
In summary, the main contributions of this paper are summarized as follows:

- 1) A model predictive framework which enables interaction between the utility and GEI for efficient black start of DS, by sharing only the coupling variables such as flexibility range and dispatch signal.
- 2) Predictive modeling of GEI with the ability to predict flexibility range and follow utility dispatch signal. With this approach, the contribution of BTM DERs on the black start is assessed for various ratio of customers with GEI and without GEI.
- 3) Predictive modeling of bottom-up BS strategy with GFM inverter's frequency security constraint, energizing and synchronizing switching constraints that enable formation and synchronization of multiple dynamic microgrids to share their energy and power capacity for faster restoration.

The remainder of the paper is organized as follows. Section II provides an overview of the proposed framework. Section III presents the predictive modeling of grid-edge intelligence. Section IV formulates the bottom-up black-start methodology. Section V presents simulation results and discussion. Section VI concludes this paper.

## II. OVERVIEW OF THE PROPOSED FRAMEWORK

As shown in Fig. 1, GEI is deployed in residential houses equipped with BTM DERs, BES, HVAC systems, and other loads. Each GEI device is capable of estimating its flexibility range and tracking dispatch signals from the utility to optimize its operation while supporting utility functions such as black start. The GEI communicates its flexibility range to the utility, which in turn sends dispatch signals back



195 Fig. 1. Overview of the proposed framework.

196 to the GEI devices for tracking. This dynamic interaction  
 197 preserves privacy, as both the GEI devices and the utility  
 198 exchange only the coupling variables rather than detailed asset  
 199 information. Additionally, both the GEI operations and the  
 200 black start process are implemented using the principles of  
 201 model predictive control (MPC).

202 The black start strategy follows a bottom-up approach. In  
 203 this setup, multiple GFM inverters initiate the black start  
 204 from different locations, forming several islanded microgrids  
 205 while establishing cranking paths to bring GFL resources  
 206 online. Unlike in transmission systems, load pickup is nec-  
 207 essary during cranking path formation in distribution systems.  
 208 This makes coordination between GEI devices and the utility  
 209 essential to ensure dynamic frequency security throughout the  
 210 restoration process.

### 211 III. PREDICTIVE MODELING OF GRID EDGE 212 INTELLIGENCE

213 In this paper, residential loads are assumed to be equipped  
 214 with GEI. Each GEI operates based on a predictive model that  
 215 communicates its flexibility range to the utility and tracks the  
 216 dispatch signal received from the utility.

217 The prediction horizon is defined relative to the current time  
 218  $t$  as  $\{t + k\Delta t : k \in \mathcal{N}_k\}$ , where  $\Delta t$  denotes the time step and  
 219  $\mathcal{N}_k = \{1, 2, \dots, N\}$ . This notation is consistently used for all  
 220 predictive models, including those for GEI and the black start  
 221 modeling in Section IV.

#### 222 A. Residential Load Model With GEI

223 A residential house with GEI is assumed to be equipped  
 224 with an HVAC system, a BES, PV, and other loads. The set  $\mathcal{N}_h$   
 225 denotes the nodes where residential houses have GEI devices.

226 1) *Thermal Modeling of Residential House With HVAC:*  
 227 The thermal dynamics model of a generic house is illustrated  
 228 in Fig. 2. The thermal model consists of five nodes, including  
 229 four wall nodes and one room node. Each node is thermally  
 230 connected to other nodes through thermal resistances and  
 231 grounded through thermal capacitance. In this section, a typi-  
 232 cal three-resistance and two-capacitance (3R–2C) model [21]

is employed to model its thermal dynamics. The wall temper-  
 233 ature  $T_{h,i}^{\text{wall}}$  is primarily influenced by the indoor temperature  
 234  $T_h^{\text{room}}$  and the outdoor temperature  $T_h^{\text{out}}$ . The temperature pro-  
 235 file of the house  $h$  with walls represented by a set  $i = \{1, 2, 3, 4\}$   
 236 can be modeled by (1), as in [22]:

$$237 C_{h,i}^{\text{wall}} \frac{T_{h,t+k}^{\text{wall}} - T_{h,t+k-1}^{\text{wall}}}{\Delta t} = \frac{T_{h,t+k}^{\text{room}} - T_{h,i,t+k}^{\text{wall}}}{R_{h,i}^{\text{wall}}} \quad 238$$

$$239 + \frac{T_h^{\text{out}} - T_{h,i,t+k}^{\text{wall}}}{R_{h,i}^{\text{wall}}} + w_{h,i}^{\text{wall}} Q_{h,i,t+k}^{\text{rad,wall}} \quad \forall i \in \{1, 2, 3, 4\} \quad 240 \quad (1) \quad 241$$

242 Here,  $C_{h,i}^{\text{wall}}$  denotes the thermal capacitance and  $R_{h,i}^{\text{wall}}$  rep-  
 243 represents the corresponding thermal resistance.  $Q_{h,i}^{\text{rad,wall}}$  is the  
 244 external radiative heat input to wall  $i$ , and  $w_{h,i}^{\text{wall}}$  is a simplified  
 245 weighting factor applied to  $Q_{h,i}^{\text{rad,wall}}$ .

246 The indoor temperature experienced by occupants is regu-  
 247 lated by the HVAC system. The thermal dynamics of the  
 248 indoor zone can be defined by constraints (2).

$$249 C_h^{\text{room}} \frac{T_{h,t+k}^{\text{room}} - T_{h,t+k-1}^{\text{room}}}{\Delta t} = \sum_{i=1}^4 \frac{T_{h,i,t+k}^{\text{wall}} - T_{h,t+k}^{\text{room}}}{R_{h,i}^{\text{wall}}} \quad 250$$

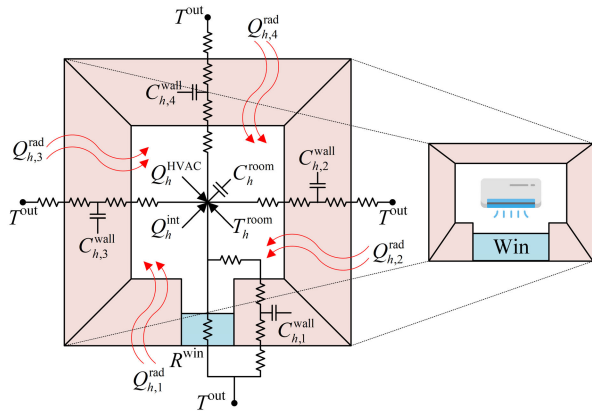
$$251 + \frac{T_h^{\text{out}} - T_{h,t+k}^{\text{room}}}{R_{h,i}^{\text{win}}} + w_{h,i}^{\text{win}} Q_{h,t+k}^{\text{rad,win}} + Q_{h,t+k}^{\text{int}} + Q_{h,t+k}^{\text{HVAC}} \quad 252 \quad (2)$$

253 Here,  $Q_h^{\text{rad,win}}$  is the external radiative heat transferring into  
 254 the room through the window, and  $w_h^{\text{win}}$  is the corresponding  
 255 weighting factor.  $Q_h^{\text{int}}$  and  $Q_h^{\text{HVAC}}$  denote the internal heat gains  
 256 and the heat supplied by the HVAC system, respectively.

257 a) *HVAC constraints:* The power consumed by the  
 258 HVAC system is determined by the temperature difference  
 259 between the HVAC setpoint temperature  $T_h^{\text{HVAC}}$  and the actual  
 260 indoor temperature  $T_h^{\text{room}}$ , and is expressed by constraint (3),  
 261 as in [11]. Constraint (4) defines the upper and lower bounds  
 262 of the HVAC temperature, denoted by  $\overline{T}_h^{\text{HVAC}}$  and  $\underline{T}_h^{\text{HVAC}}$ ,  
 263 respectively.

$$264 P_{h,t+k}^{\text{HVAC}} = \left[ \frac{T_{h,t+k}^{\text{HVAC}} - T_{h,t+k}^{\text{room}}}{\text{COP}(273 + T_{h,t+k}^{\text{room}})} \right] Q_{h,t+k}^{\text{HVAC}} \quad 265 \quad (3)$$

$$266 \underline{T}_h^{\text{HVAC}} \leq T_{h,t+k}^{\text{HVAC}} \leq \overline{T}_h^{\text{HVAC}} \quad 266 \quad (4)$$



267 Fig. 2. RC model of a generic house.

268 2) *BES Constraints*: The energy storage of the BES dynam-  
 269 ically changes with charging and discharging power, and  
 270 it is governed by constraint (5). Constraint (6) defines the  
 271 maximum and minimum energy storage capacities of the BES,  
 272 denoted by  $\bar{E}_h^{ES}$  and  $\underline{E}_h^{ES}$ , respectively. Constraints (7) and  
 273 (8) ensure that the charging power  $P_h^{ES,C}$  and discharging  
 274 power  $P_h^{ES,D}$  do not exceed the maximum charging capacity  
 275  $\bar{P}_h^{ES,C}$  and discharging capacity  $\bar{P}_h^{ES,D}$ , respectively. Similarly,  
 276 the charging and discharging ramp limits are defined by  
 277 constraints (9) and (10). Constraint (11) defines that the BES  
 278 cannot be charged and discharged simultaneously.

$$280 E_{h,t+k}^{ES} = E_{h,t+k-1}^{ES} + \Delta t \left( \eta_h^{ES,C} P_{h,t+k}^{ES,C} - \frac{P_{h,t+k}^{ES,D}}{\eta_h^{ES,D}} \right) \quad (5)$$

$$282 \underline{E}_h^{ES} \leq E_{h,t+k}^{ES} \leq \bar{E}_h^{ES} \quad (6)$$

$$283 0 \leq P_{h,t+k}^{ES,C} \leq \beta_{h,t+k}^{ES,C} \bar{P}_h^{ES,C} \quad (7)$$

$$284 0 \leq P_{h,t+k}^{ES,D} \leq \beta_{h,t+k}^{ES,D} \bar{P}_h^{ES,D} \quad (8)$$

$$285 \underline{\Delta P}_h^{ES,C} \leq \Delta P_{h,t+k}^{ES,C} \leq \bar{\Delta P}_h^{ES,C} \quad (9)$$

$$286 \underline{\Delta P}_h^{ES,D} \leq \Delta P_{h,t+k}^{ES,D} \leq \bar{\Delta P}_h^{ES,D} \quad (10)$$

$$287 \beta_{h,t+k}^{ES,C} + \beta_{h,t+k}^{ES,D} \leq 1 \quad (11)$$

288 Here,  $\eta_h^{ES,C}$  and  $\eta_h^{ES,D}$  are BES charging and discharging  
 289 efficiencies.  $\underline{\Delta P}_h^{ES,C}/\bar{\Delta P}_h^{ES,C}$  and  $\bar{\Delta P}_h^{ES,D}/\bar{\Delta P}_h^{ES,D}$  are minimum  
 290 and maximum charging/discharging rates.  $\beta_{h,t+k}^{ES,C}$  and  $\beta_{h,t+k}^{ES,D}$  are  
 291 binary variables.

292 3) *PV Constraints*: The PV is modeled using multi-time-  
 293 step forecasted values  $\tilde{P}_{h,t+k}^{PV}$  over the current prediction  
 294 horizon. Accordingly, the PV output active power is defined  
 295 as:

$$296 P_{h,t+k}^{PV} = \tilde{P}_{h,t+k}^{PV} x_{h,t+k}^{PV} \quad (12)$$

297 where  $x_{h,t+k}^{PV}$  is an adjustable scaling factor constrained by  
 298  $0.5 \leq x_{h,t+k}^{PV} \leq 1$ .

299 4) *Load Constraints*: The load is also modeled using pre-  
 300 dicted values  $\tilde{P}_{h,t+k}^{load}$  along the current prediction horizon and  
 301 is defined as:

$$302 P_{h,t+k}^{load} = \tilde{P}_{h,t+k}^{load} x_{h,t+k}^{load} \quad (13)$$

303 where  $x_{h,t+k}^{load}$  is an adjustable scaling factor constrained by  
 304  $0.5 \leq x_{h,t+k}^{load} \leq 1$ .

## B. GEI Functions

305 This section primarily focuses on two key functions of GEI:  
 306 (a) flexibility range estimation and (b) energy optimization  
 307 during both standalone and grid-connected operations. Other  
 308 functions, such as forecasting and coordination, are illustrated  
 309 in Fig. 3.

310 1) *Flexibility Range Estimation*: GEI analyzes the power  
 311 consumption of all BTM DERs, loads, and the overall power  
 312 consumption of the house. GEI estimates the net power  
 313 consumption of a house  $h$  as:

$$314 P_{h,t+k}^{GEI} = P_{h,t+k}^{ES,C} - P_{h,t+k}^{ES,D} - P_{h,t+k}^{PV} + P_{h,t+k}^{load} + P_{h,t+k}^{HVAC} \quad (14)$$

315 The flexibility range is defined by the upper bound  $\bar{P}_{h,t+k}^{GEI}$   
 316 and the lower bound  $\underline{P}_{h,t+k}^{GEI}$ . Along the prediction horizon, it  
 317 can be obtained by solving the optimization problems defined  
 318 in (15) and (16).

$$319 \bar{P}_{h,t+k}^{GEI} = \arg \max \sum_{k \in \mathcal{N}_k} P_{h,t+k}^{GEI} \quad (15)$$

320  
321  
322

$$323 \underline{P}_{h,t+k}^{GEI} = \arg \min \sum_{k \in \mathcal{N}_k} P_{h,t+k}^{GEI} \quad (16)$$

324  
325

326 2) *Energy Optimization*: The GEI optimizes the energy  
 327 consumption during standalone operation, whereas it tracks  
 328 the dispatch signal ( $P_{h,t+k}^{dis}$ ) when connected with the grid. We  
 329 define the grid connection status by a binary variable  $\beta^{GEI}$ , to  
 330 express the generic objective of GEI as:

$$331 \min \sum_{k \in \mathcal{N}_k} \left[ (1 - \beta_h^{GEI}) P_{h,t+k}^{GEI} \right. \\ \left. + \beta_h^{GEI} \| P_{h,t+k}^{GEI} - P_{h,t+k}^{dis} \|^2 \right] \quad (17)$$

332  
333  
334

335 Here, when  $\beta_h^{GEI} = 1$ , the GEI is grid connected and follows the  
 336 utility dispatch signal; and when  $\beta_h^{GEI} = 0$ , the GEI continues  
 337 to operate in a consumption-minimizing mode.

## C. GEI-Utility Coordination

338 The proposed dynamic interaction between the utility and  
 339 GEI is illustrated in Fig. 3. This coordination allows the  
 340 utility and numerous GEI devices to collaboratively support  
 341 the restoration process by exchanging only flexibility ranges  
 342 and dispatch signals. As a result, neither the utility nor the  
 343 GEI devices are required to share detailed asset information  
 344 with one another.

345 The process begins with the utility gathering fault and  
 346 outage data, along with forecasts for DER generation and load  
 347 demand. At the same time, each GEI estimates its flexibility  
 348 range using forecasted DER output and load consumption.  
 349 This flexibility range is then communicated to the utility.  
 350 Based on the received flexibility ranges, the utility optimizes  
 351 the restoration plan, reconfigures the distribution system, and  
 352 issues dispatch signals to the GEI devices.

353 Each GEI follows the assigned dispatch signal when con-  
 354 nected to the utility. If a GEI is not yet connected during  
 355

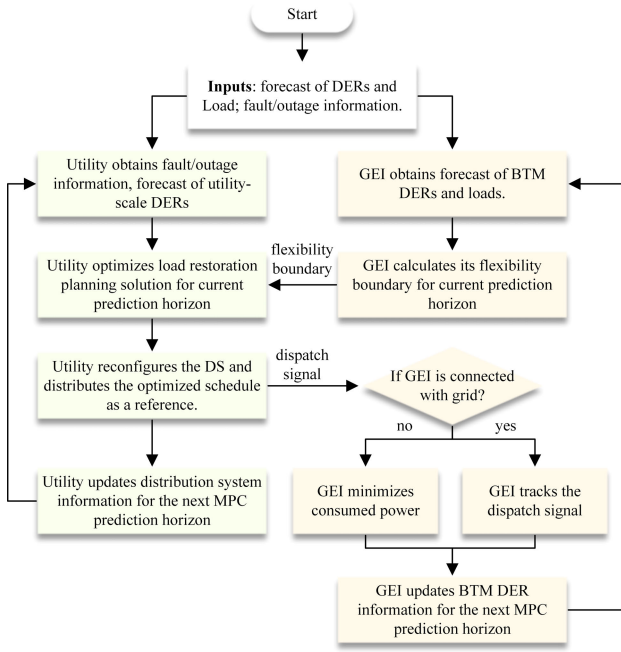


Fig. 3. GEI and utility functions and their proposed coordination.

restoration, it operates in a standalone mode, minimizing its energy consumption. Finally, each GEI updates its BTM DER information in preparation for the next prediction horizon.

#### IV. PREDICTIVE MODELING BLACK START OF DISTRIBUTION SYSTEM

This section presents a predictive model for the bottom-up black start strategy, incorporating frequency security constraints, switching constraints, and synchronization switching constraints. The black start model is then formulated as a mixed-integer problem to maximize load restoration.

##### A. Formulation

The objective is to maximize the total load restoration over the  $\mathcal{N}_k$  for each time  $t$ , which is formulated as:

$$\begin{aligned} \max \sum_{k \in \mathcal{N}_k} \sum_{i \in \mathcal{N}_i} \sum_{p \in \mathcal{N}_p} P_{i,p,k}^D \Delta t \quad (18) \\ \text{s.t. (19) ~ (53)} \end{aligned}$$

Here,  $\mathcal{N}_i$  and  $\mathcal{N}_p$  represent sets of load buses and phases.  $P^D$  denotes active power restored.

##### B. GFM-BESS Constraints

The typical structure of the virtual synchronous generator (VSG) control is illustrated in Fig. 4. VSG control is a grid-forming strategy that emulates the dynamic behavior of a synchronous generator, providing both frequency and voltage support. As illustrated in Fig. 4, a typical VSG-based GFMI employs two loops: (i) **P-f loop**: the frequency error ( $f^* - f$ ) drives a swing dynamics parameterized by virtual inertia  $H$  and damping  $D$ , providing inertial and damping responses to active-power imbalances; (ii) **Q-V loop**: voltage

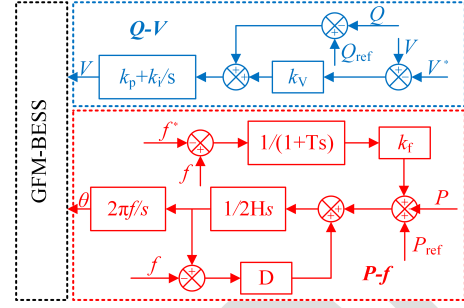


Fig. 4. VSG-based control of GFMI.

droop regulates the terminal voltage toward  $V^*$  by modulating reactive power  $Q$ , enabling voltage support. In this work, all GFM-BESS are equipped with VSG control. The set  $\mathcal{N}_R$  denotes the location of nodes with GFM-BESS. To ensure compatibility with the branch flow model, a new voltage variable is introduced as  $v = |V|^2$ , where  $|V|$  denotes the voltage magnitude.

The voltage magnitude deviation  $\Delta v_{i,p,k}$  and frequency deviation  $\Delta f_{i,k}^{\text{QSS}}$  of the GFM-BESS at QSS are defined by constraints (19) and (20), as described in [10]:

$$v_{i,p,t+k} = (V^*)^2 + \Delta v_{i,t+k}^{\text{cc}} \quad (19)$$

$$\Delta f_{i,t+k}^{\text{QSS}} = f^* \frac{\sum_{p \in \mathcal{N}_p} \Delta P_{i,p,t+k}^{\text{ES}}}{S_i^{\text{rat}} (D_i + k_i^f)} \quad (20)$$

The upper and lower bounds for these deviations are constrained by (21) and (22), respectively:

$$-0.0975(V^*)^2 \leq \Delta v_{i,p,k} \leq 0.1025(V^*)^2 \quad (21)$$

$$\Delta \underline{f}_i^{\text{QSS}} \leq \Delta f_{i,t+k}^{\text{QSS}} \leq \Delta \overline{f}_i^{\text{QSS}} \quad (22)$$

where  $V^*$  and  $f^*$  represent the nominal voltage and frequency references, respectively. The  $S^{\text{rat}}$  is the rated capacity of the inverter.  $\Delta \underline{f}_i^{\text{QSS}}$  and  $\Delta \overline{f}_i^{\text{QSS}}$  denote the minimum and maximum frequency deviations at QSS.

In addition, the dynamic energy storage behavior of the GFM-BESS is modeled by constraint (23). The active power  $P_{i,p}^{\text{ES}}$  and reactive power  $Q_{i,p}^{\text{ES}}$  of the inverter are limited by the rated capacity, as shown in constraint (24):

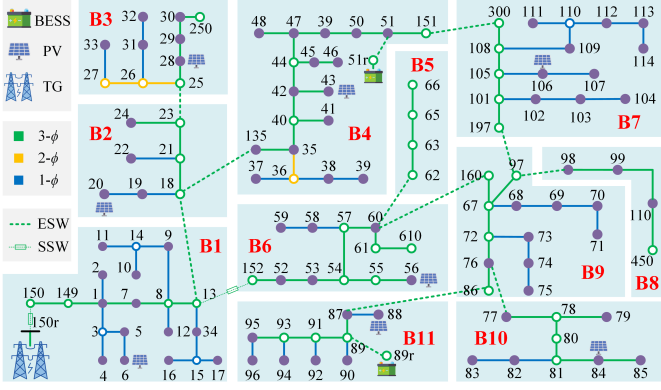
$$E_{i,t+k}^{\text{ES}} = E_{i,t+k-1}^{\text{ES}} + \Delta t \sum_{p \in \mathcal{N}_p} \Delta P_{i,p,t+k}^{\text{ES}} \quad (23)$$

$$\max_{p \in \mathcal{N}_p} \{ (P_{i,p,t+k}^{\text{ES}})^2 + (Q_{i,p,t+k}^{\text{ES}})^2 \} \leq \left( \frac{1}{3} S_i^{\text{rat}} \right)^2 \quad (24)$$

1) **Frequency Security Constraints**: To model the frequency response of GFM-BESS during load restoration, constraints (25) and (26) are employed to calculate the RoCoF and the frequency nadir deviation  $\Delta f_{i,k}^{\text{nad}}$  at QSS, respectively:

$$f_{i,t+k}^{\text{RoCoF}} = \frac{\sum_{p \in \mathcal{N}_p} \Delta P_{i,p,t+k}^{\text{ES}}}{2S_i^{\text{rat}} H_i} \quad (25)$$

$$\Delta f_{i,t+k}^{\text{nad}} = f^* \frac{\sum_{p \in \mathcal{N}_p} \Delta P_{i,p,t+k}^{\text{ES}}}{S_i^{\text{rat}} (D_i + k_i^f)} (1 + \gamma_i) \quad (26)$$



423 Fig. 5. Modified IEEE-123 bus distribution system.

424 Constraints (27) and (28) define the boundaries for  
425 the RoCoF  $f_{i,k}^{\text{RoCoF}}$  and frequency nadir deviations of the  
426 GFM-BESS, respectively:

$$427 \quad \underline{f}_i^{\text{RoCoF}} \leq f_{i,t+k}^{\text{RoCoF}} \leq \bar{f}_i^{\text{RoCoF}} \quad (27)$$

$$428 \quad \Delta \underline{f}_i^{\text{nadir}} \leq \Delta f_{i,t+k}^{\text{nadir}} \leq \Delta \bar{f}_i^{\text{nadir}} \quad (28)$$

429 where  $\underline{f}_i^{\text{RoCoF}}/\bar{f}_i^{\text{RoCoF}}$  and  $\Delta \underline{f}_i^{\text{nadir}}/\Delta \bar{f}_i^{\text{nadir}}$  represent the lower  
430 and upper bounds of RoCoF and frequency nadir deviations,  
431 respectively.

432 2) *Synchronization Constraints*: During the synchroniza-  
433 tion period, the frequency among different GFM-BESS can  
434 be aligned by adjusting their reference frequency, represented  
435 by  $\Delta f^*$ . Constraint (29) allows for frequency penetration  
436 in GFM-BESS units attempting to synchronize with other  
437 GFM-BESS, while constraint (30) defines the acceptable  
438 boundaries for this frequency penetration.

$$439 \quad f_{i,t+k} = f^* \left( 1 - \frac{\sum_{p \in \mathcal{N}_p} P_{i,p,t+k}^{\text{ES}}}{S_i^{\text{rat}}(D_i + k_i^f)} \right) + \Delta f_{i,t+k}^* \sum_{b \in \mathcal{N}_R} \delta_{b,t+k} \quad (29)$$

$$441 \quad \Delta \underline{f}_i^{\text{syn}} \leq \Delta f_{i,t+k}^* \leq \Delta \bar{f}_i^{\text{syn}} \quad (30)$$

442 where  $\delta_b$  is a binary variable and  $\Delta f_i^*$  represents frequency  
443 penetration.  $\delta_b$  is set as 1 only during the synchronization  
444 period.  $\Delta \underline{f}_i^{\text{syn}}$  and  $\Delta \bar{f}_i^{\text{syn}}$  are the lower and upper bounds of  
445 frequency penetration, respectively.

### 446 C. Switching Constraints

447 DS generally has multiple bus blocks, as shown in Fig. 5,  
448 interconnected by two types of switches: energizing switches  
449 (ESWs) and synchronizing switches (SSWs). ESWs are used  
450 to energize inactive sections of the distribution system, while  
451 SSWs ensure frequency synchronization when interconnecting  
452 two islanded microgrids. We define all ESWs by the set  $\mathcal{W}_{\text{ESW}}$   
453 and all SSWs by the set  $\mathcal{W}_{\text{SSW}}$ . All switches are modeled by  
454 a negligible-impedance line  $(i, j)$  where  $i, j \in \mathcal{N}$ .

455 1) *Energizing Switch*: We define the active/inactive status  
456 of the switch by a binary variable  $y^L$ . The switching conditions  
457 for all ESWs  $(i, j) \in \mathcal{W}_{\text{ESW}}$  can be defined as:

$$458 \quad y_{ij,t+k}^L \leq y_{i,t+k-1}^B + y_{j,t+k-1}^B \quad (31)$$

$$459 \quad 0 \leq \Delta y_{ij,t+k}^L \leq 2 - y_{i,t+k-1}^B - y_{j,t+k-1}^B \quad (32)$$

460 where  $\Delta y_{ij,t+k}^L = y_{ij,t+k}^L - y_{ij,t+k-1}^L$ . Constraint (31) ensures that  
461 an ESW can only close if at least one of the buses is in an  
462 active state defined by  $y^B$ . Another constraint (32) prevents the  
463 ESW from closing if both connected buses are in an active  
464 state.

465 2) *Synchronizing Switch*: The switching constraint for  
466 ESWs can be defined for all  $(i, j) \in \mathcal{W}_{\text{ESW}}$  as:

$$467 \quad y_{ij,t+k}^L \leq y_{i,t+k-1}^B + y_{j,t+k-1}^B \quad (33)$$

$$468 \quad z_{ij,t+k}^L = \Delta y_{ij,t+k}^L (y_{i,t+k-1}^B + y_{j,t+k-1}^B - y_{ij,t+k}^L) \quad (34)$$

$$469 \quad -(1 - z_{ij,t+k}^L)M - \epsilon \leq P_{ij,t+k} \leq \epsilon + (1 - z_{ij,t+k}^L)M \quad (35)$$

$$470 \quad -(1 - z_{ij,t+k}^L)M - \epsilon \leq Q_{ij,t+k} \leq \epsilon + (1 - z_{ij,t+k}^L)M \quad (36)$$

$$471 \quad -(1 - y_{ij,t+k}^L)M - \epsilon \leq f_{i,t+k} - f_{j,t+k}$$

$$472 \quad \leq \epsilon + (1 - y_{ij,t+k}^L)M \quad (37)$$

473 where  $M$  and  $\epsilon$  are big and small numbers. Constraint (33)  
474 ensures that an SSW can be closed even when the connecting  
475 buses are both active. Constraint (34) defines the instant when  
476 the SSW is closed. Constraints (35) and (36) ensure that the  
477 power flow through the SSW is zero during the instant of  
478 closing the SSW to ensure that the voltage and angle of the  
479 connecting buses are sufficiently close. Constraint (37) ensures  
480 that the frequencies of the two islanded zones are matched  
481 prior to interconnection.

### 482 D. Bus Blocks Energizing Constraints

483 The set of bus blocks is defined by  $\mathcal{B}$ , and the switches  
484 associated with each bus block  $b \in \mathcal{B}$  are defined by the set  
485  $\mathcal{W}_b$ . The energizing constraints for each bus block are modeled  
486 as follows.

$$487 \quad y_{b,t+k}^{BB} \geq y_{ij,t+k}^L, \forall \{b \in \mathcal{B} \mid (i, j) \in \mathcal{W}_b\} \quad (38)$$

$$488 \quad y_{b,t+k}^{BB} \geq y_{b,t+k-1}^{BB}, \forall b \in \mathcal{B} \quad (39)$$

$$489 \quad y_{ij,t+k}^L = y_{b,t+k}^{BB}, \forall \{b \in \mathcal{B} \mid (i, j) \in \mathcal{L}_b\} \quad (40)$$

$$490 \quad y_{i,t+k}^B = y_{b,t+k}^{BB}, \forall \{b \in \mathcal{B} \mid i \in \mathcal{N}_b\} \quad (41)$$

$$491 \quad \sum_{(i,j) \in \mathcal{W}_b} y_{ij,t+k}^L - \sum_{(i,j) \in \mathcal{W}_b} y_{ij,t+k-1}^L \leq M y_{b,t+k}^{BB} + 1, \forall b \in \mathcal{B} \quad (42)$$

493 Here,  $\mathcal{L}_b$  and  $\mathcal{N}_b$  are the set of lines and nodes associated  
494 with bus block  $b$ . Constraint (38) ensures that a bus block  
495 becomes active only if at least one switch connected to it  
496 has been activated. Constraint (39) guarantees that once a bus  
497 block is energized, it remains energized in all subsequent time  
498 steps. Constraint (40) ensures that the energizing of a bus  
499 block activates all lines within that block. The restriction (41)  
500 ensures that the energizing of a bus block activates all buses  
501 within that block. The restriction (42) restricts the number of  
502 switches that can be activated at any time step for each bus  
503 block, specifically differentiating between active and inactive  
504 bus blocks.

### 505 E. Linear Power Flow Model Adaptive to Network Topology

506 A linearized model for a three-phase unbalanced system, as  
507 proposed in [23], is leveraged to develop a switching-enabled  
508 power flow formulation.

509 1) *Power Constraints*: Constraints (43) and (44) impose  
 510 big-M constraints on active and reactive power flows ( $P_{ij}$  and  
 511  $Q_{ij}$ ) of line  $(i, j)$ , ensuring that the power flow is allowed only  
 512 when the line is active, as indicated by the binary variable  $y_{ij}^L$ .  
 513 Constraints (45) and (46) define the nodal power balance.

$$514 -M^{\mathcal{N}_{ip}} y_{ij,t+k}^L \leq P_{ij,t+k} \leq M^{\mathcal{N}_{ip}} y_{ij,t+k}^L \quad (43)$$

$$515 -M^{\mathcal{N}_{ip}} y_{ij,t+k}^L \leq Q_{ij,t+k} \leq M^{\mathcal{N}_{ip}} y_{ij,t+k}^L \quad (44)$$

$$516 P_{ij,t+k} = \sum_{l \in \mathcal{N}_j} P_{jl,t+k} + p_{j,t+k} \quad (45)$$

$$517 Q_{ij,t+k} = \sum_{l \in \mathcal{N}_j} Q_{jl,t+k} + q_{j,t+k} \quad (46)$$

519 2) *Voltage Constraints*: Constraint (47) ensures that the  
 520 nodal voltage of energized nodes is within the safe range.  
 521 Constraints (48) and (49) describe the voltage difference  
 522 between two end nodes of each connected line.

$$523 0.9025^{\mathcal{N}_{ip}} v_{j,t+k}^B \leq v_{j,t+k} \leq 1.1025^{\mathcal{N}_{ip}} v_{j,t+k}^B \quad (47)$$

$$524 v_{j,t+k} \leq v_{i,t+k}^{\mathcal{N}_{ip}} - 2(\bar{R}_{ij} P_{ij,t+k} + \bar{X}_{ij} Q_{ij,t+k})$$

$$525 + M^{\mathcal{N}_{ip}} (1 - y_{ij,t+k}^L) \quad (48)$$

$$526 v_{j,t+k} \geq v_{i,t+k}^{\mathcal{N}_{ip}} - 2(\bar{R}_{ij} P_{ij,t+k} + \bar{X}_{ij} Q_{ij,t+k})$$

$$527 - M^{\mathcal{N}_{ip}} (1 - y_{ij,t+k}^L) \quad (49)$$

528 where  $P_{ij}$  and  $Q_{ij}$  are the active and reactive power on line  
 529  $(i, j)$ .  $M$  is a big number for the relaxation of power flow  
 530 constraints.  $\mathcal{N}_j$  is the set of downstream nodes connected from  
 531 node  $j$ .  $\bar{R}_{ij}$  and  $\bar{X}_{ij}$  denote the resistance and reactance matrices  
 532 of the line  $(i, j)$ .

### 533 F. GFL Inverter and GEI Constraints

534 We adopt GFL inverters, such as PVs, from [10], but do not  
 535 discuss them explicitly due to space limitations. Each GEI  $h$   
 536 provides a flexibility range ( $P_{h,t+k}^{\text{GEI}}, \bar{P}_{h,t+k}^{\text{GEI}}$ ) to the utility, which  
 537 introduces a new constraint in the proposed framework. This  
 538 constraint is defined for all  $h \in \mathcal{N}_h$  as:

$$539 \underline{P}_{h,t+k}^{\text{GEI}} \leq P_{h,t+k}^{\text{dis}} \leq \bar{P}_{h,t+k}^{\text{GEI}} \quad (50)$$

540 Here,  $P^{\text{dis}}$  is a dispatch signal communicated to the GEI  
 541 device.

### 542 G. Modeling Transmission Grid Outage and Recovery

543 During the BS process, the DS is disconnected from an out-  
 544 of-service TG and subsequently reconnected once the TG has  
 545 been restored. The constraints related to the TG are modeled  
 546 as follows:

$$547 (P_{g,t+k}^{\text{TG}})^2 + (Q_{g,t+k}^{\text{TG}})^2 \leq (S^{\text{rat}})^2 \quad (51)$$

$$548 1.0 y_{g,t+k}^{\text{TG}} \geq v_{g,t+k} \geq 1.0 y_{g,t+k}^{\text{TG}} \quad (52)$$

$$549 60 y_{g,t+k}^{\text{TG}} \geq f_{g,t+k} \geq 60 y_{g,t+k}^{\text{TG}} \quad (53)$$

550 Constraint (51) defines the thermal power limit of the  
 551 distribution substation. Constraints (52) and (53) define the  
 552 voltage and frequency values of the TG, respectively. By  
 553 parameterizing  $y_g^{\text{TG}}$ , the active/inactive status of TG can be  
 554 simulated.

TABLE II  
THE DERs PARAMETERS

DER	Capacity	Location	DER	Capacity	Location
PV1	24.5kW	6	PV2	44.1kW	20
PV3	24.5kW	28	PV4	24.5kW	43
PV5	24.5kW	56	PV6	12.25kW	84
PV7	24.5kW	88	PV8	24.5kW	106
BESS1	24.5kW	51r	BESS2	24.5kW	89r

TABLE III  
THE SWITCH PARAMETERS

Switch	Location	Type	Switch	Location	Type
S1	(13, 18)	ESW	S2	(18, 135)	ESW
S3	(23, 25)	ESW	S4	(151, 300)	ESW
S5	(51r, 51)	ESW	S6	(60, 62)	ESW
S7	(13, 152)	SSW	S8	(60, 160)	ESW
S9	(97, 197)	ESW	S10	(97, 98)	ESW
S10	(76, 77)	ESW	S12	(86, 87)	ESW
S13	(89r, 89)	ESW	S14	(150r, 150)	SSW

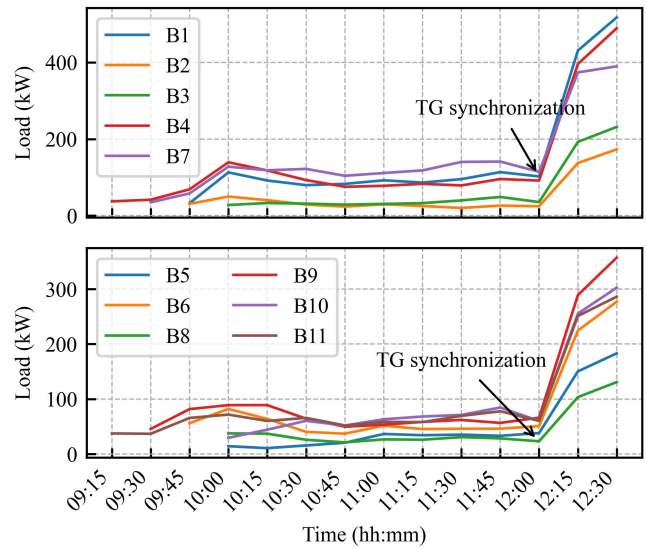
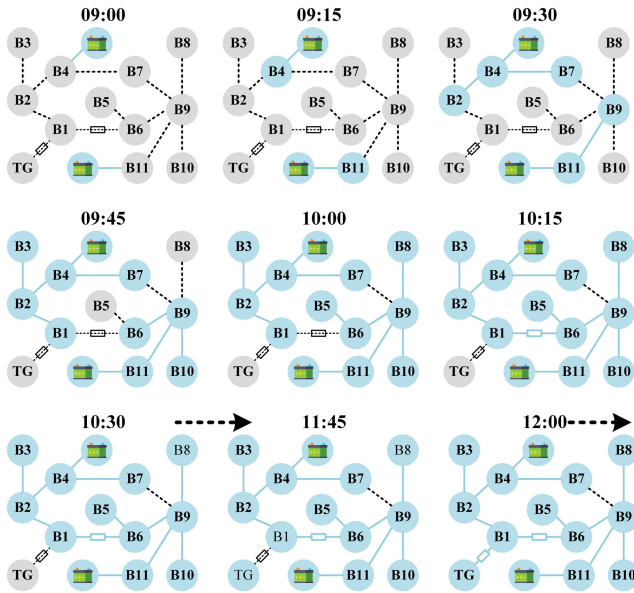
## 559 V. RESULTS

560 This section evaluates the performance of the proposed  
 561 predictive framework for the GEI-assisted bottom-up black  
 562 start strategy in the modified IEEE 123-bus DS. A blackout is  
 563 simulated by the outage of the TG, followed by its recovery  
 564 after a few hours. During this period, the proposed framework  
 565 demonstrates black start and restoration by forming multiple  
 566 MGs with the help of GFM and GFL inverters and the  
 567 GEI devices. Detailed results are presented for a study with  
 568 100% GEI, highlighting the prediction of flexibility ranges,  
 569 interaction with the utility, and tracking of the dispatch sig-  
 570 nal. Additionally, the sequential formation of cranking paths,  
 571 starting from the GFM and continuing until the energization of  
 572 all bus blocks across multiple MGs, is shown to comply with  
 573 dynamic frequency security limits. A comparative analysis for  
 574 various levels of GEI in the IEEE feeder is also presented  
 575 to highlight the contribution of GEI in system black start  
 576 and restoration. The proposed formulation is of mixed-integer  
 577 nature with a linear objective and a few quadratic constraints,  
 578 solved using Gurobi 11.0.3.

### 579 A. Test System and Framework Parameters

580 As depicted in Fig. 5, the modified IEEE 123-bus distribu-  
 581 tion system consists of 88 load nodes, 8 GFL PVs, and 2 GFM  
 582 BESS units. In this system, residential loads are equipped with  
 583 GEI devices capable of communicating their flexibility ranges  
 584 to the utility and following dispatch signals during a black  
 585 start, as introduced in Section III-B. The sizes and locations of  
 586 the PVs and BESS are provided in Table II. The entire system  
 587 is divided into 11 bus blocks, which are interconnected through  
 588 either an ESW or an SSW. The bus blocks are labeled in red  
 589 text, and their structure is illustrated in Fig. 5. The locations  
 590 of the SSWs and ESWs are listed in Table III.

591 Each house with GEI is equipped with a 5–7 kW rooftop PV  
 592 system and a 3–8 kW HVAC unit. The BESS has a capacity



593 Fig. 6. Sequential establishment of cranking paths in BS process.

Fig. 7. Restoration of loads in the proposed method.

628

594 ranging from 15 to 20 kWh, with an initial SoC randomly  
 595 set between 40% and 50%. In addition, the peak load of each  
 596 GEI ranges from 13 to 18 kW. These parameters are randomly  
 597 selected to model all the houses with GEI.

598 Both the GEI and the utility's black start functions are  
 599 implemented using MPC with a prediction horizon of 3 hours  
 600 and a time step of 15 minutes.

### 601 B. Black Start With 100% GEI

602 1) *Utility-Level Analysis*: The proposed framework is stud-  
 603 ied under a blackout scenario caused by TG failure, with the  
 604 TG recovering at 11:45. The BS process begins at 9:00 and  
 605 continues until the DS is synchronized with the TG at 12:00.  
 606 The sequential establishment of cranking paths during the BS  
 607 process, obtained from the proposed framework, is shown in  
 608 Fig. 6.

609 Initially, all bus blocks are inactive and disconnected, with  
 610 all switches in the open position. The BS starts with the  
 611 activation of two GFM-based BESS units at buses 51r and 89r,  
 612 forming two islanded MGs. Subsequently, neighboring bus  
 613 blocks are energized one after another with support from these  
 614 GFM-based BESS units. For example, at 9:15, bus blocks B4  
 615 and B11 are energized by closing the ESWs adjacent to the  
 616 respective BESS units. Then, at 9:30, bus blocks B2 and B7 are  
 617 energized within the first MG, while bus block B9 is energized  
 618 within the second MG. Both islanded MGs continue to expand  
 619 their boundaries until all bus blocks are energized by 10:00.  
 620 At 10:15, the SSW between bus blocks B1 and B6 is closed,  
 621 merging the two islanded MGs into a unified microgrid. At  
 622 11:45, the TG is restored but remains disconnected from the  
 623 islanded DS. Finally, at 12:00, synchronization between the  
 624 TG and DS completes the BS process, and the system operates  
 625 continuously in this final configuration. The loads served on  
 626 various bus blocks after energization are shown in Fig. 7.  
 627 For instance, the load on bus block B5 is not served by the

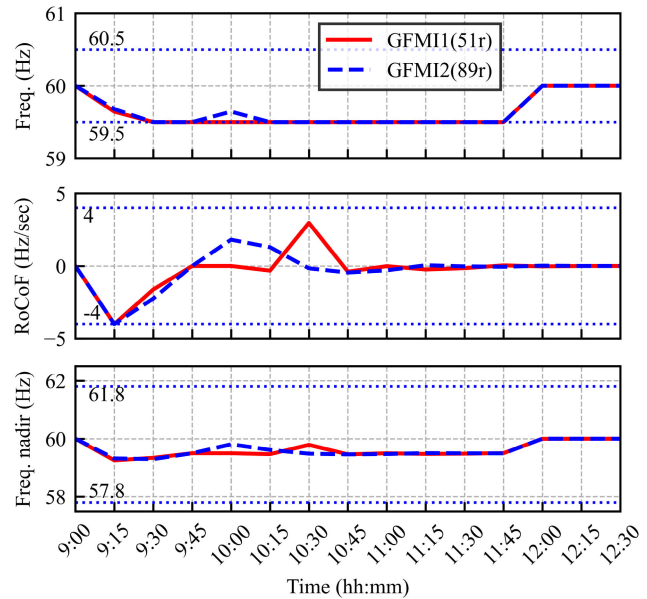
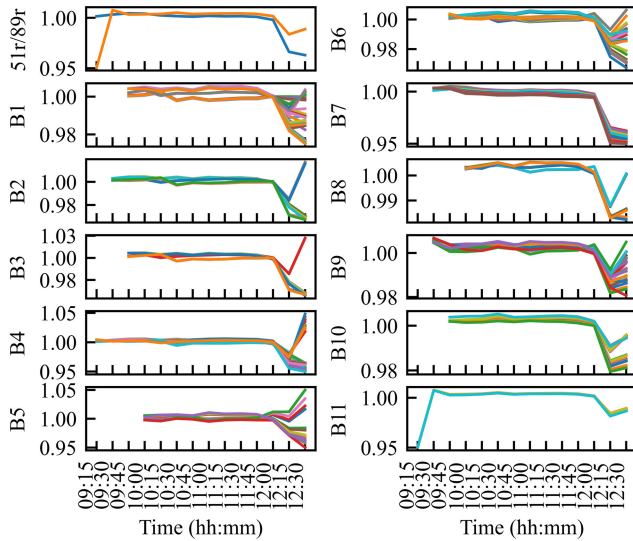


Fig. 8. Frequency responses of GFM-based BESS.

629

630 utility until 10:00 and is served afterward. In this case study  
 631 with 100% GEI, the load served by the utility is based on  
 632 the mutual interaction between the utility's capacity and the  
 633 flexibility range of GEI. This interaction is discussed in a  
 634 later part of this section. After TG synchronization, DS is  
 635 able to serve more load than during the outage period, as  
 636 seen in Fig. 7.

637 During the entire BS process, the frequency responses  
 638 of the GFM-based BESS units remained within the defined  
 639 frequency security constraints, as shown in Fig. 8. At 9:00,  
 640 when the GFM-based BESS units are started, they operate at  
 641 60 Hz since no loads are picked up at that moment. Their  
 642 frequencies gradually and independently decline as they begin  
 643 picking up loads, continuing until 10:00. At 10:15, the BESS



644 Fig. 9. Nodal voltage magnitudes at bus-blocks in the proposed method.

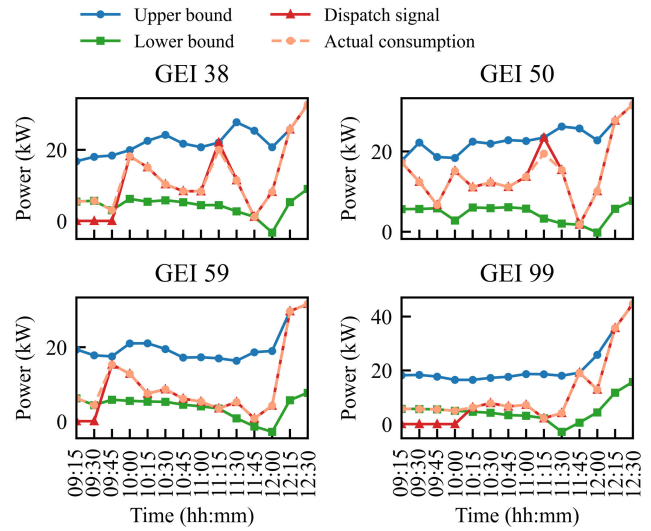
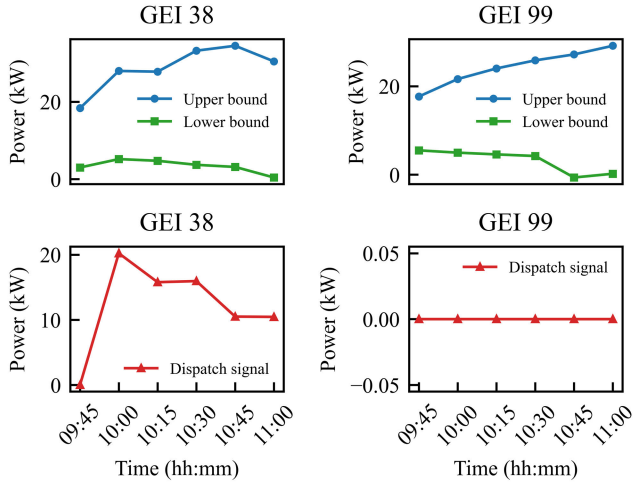


Fig. 11. Coordinated operation of GEI 38,50, 59, and 90 with the utility during BS and restoration period.



645 Fig. 10. Flexibility Ranges and Dispatch Signals of GEI 38 and 99 at 9:45.

646 units are synchronized, and their frequencies closely follow  
 647 each other for the remainder of the process. Notably, their  
 648 frequencies return to 60 Hz at 12:00 upon synchronization  
 649 with the TG. In the same figure, both  $RoCoF$  and  $f^{nad}$  remain  
 650 within acceptable limits, indicating a smooth establishment of  
 651 cranking paths without violating dynamic frequency security  
 652 constraints. In addition, the node voltages on each bus block  
 653 are within 0.95 to 1.05 p.u. throughout the BS process, as  
 654 shown in Fig. 9. As different bus blocks B1-B11 are picked  
 655 up at different time instants, their nodal voltages appear only  
 656 after energization, as seen in Fig. 9.

657 2) *Utility and GEI Interaction*: There is a continuous inter-  
 658 action between the utility and the GEI devices. For brevity,  
 659 we will only present the interaction between GEI 38 and  
 660 GEI 99 with the utility just before 9:45. A flexibility range  
 661 along the prediction horizon from 9:45 to 11:00 communi-  
 662 cated by GEI 38 and 99 is shown in two top subplots of  
 663 Fig. 10. Utility utilizes these flexibility ranges and provides

664 a dispatch signal across the prediction horizon to each GEI,  
 665 out of which the dispatch signal for GEI 38 and 99 is shown  
 666 in the two bottom subplots of Fig. 10. Since GEI 99 is  
 667 not yet connected to the utility at 9:45, the dispatch signal  
 668 is zero.

669 3) *GEI-Level Analysis*: The GEI is designed for stan-  
 670 dalone operation during a utility blackout, operating at a  
 671 minimum power level to ensure longevity. Once connected  
 672 to the utility, it begins to track the dispatch signal. In  
 673 addition, it keeps on communicating the flexibility range  
 674 at every time step. In this way, the GEI serves a dual  
 675 purpose: (1) supporting the utility in the BS process  
 676 through flexible operation, and (2) meeting its own load  
 677 requirements.

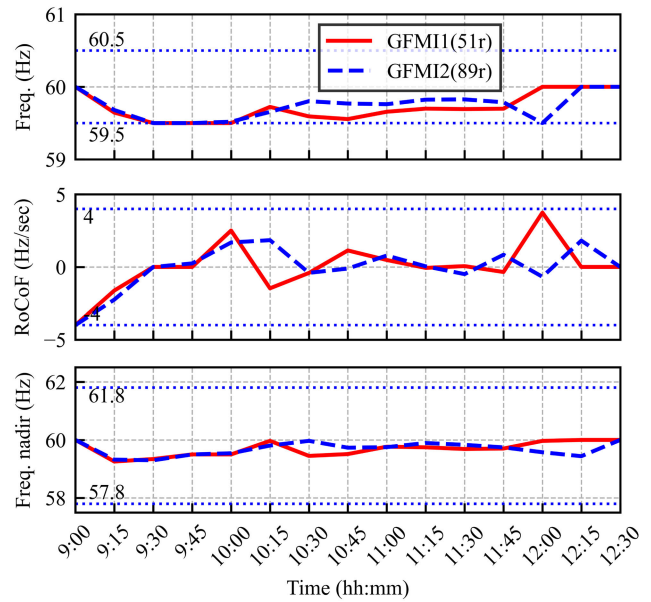
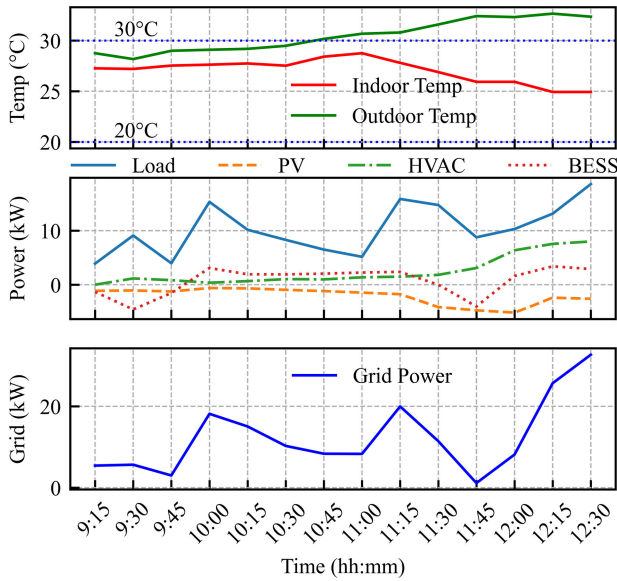
678 The high-level operation of four randomly selected GEI  
 679 devices—GEI 38, GEI 50, GEI 59, and GEI 99—is shown in  
 680 Fig. 11. GEI 38 and GEI 59 operate close to the lower bound  
 681 of their flexibility range before connecting to the utility, as  
 682 observed prior to 10:00 and 9:45, respectively. In the same  
 683 time frame, the dispatch signal is zero. Once connected to  
 684 the utility, they closely follow the dispatch signal, represented  
 685 by the red line in Fig. 11. It is important to note that the  
 686 dispatch signal always remains within the GEI’s flexibility  
 687 range due to coordinated operation between the utility and  
 688 the GEI. Similarly, GEI 50 and GEI 99 are already connected  
 689 to the utility by 9:15 and continue to track the dispatch signal  
 690 throughout the BS process.

691 Then, GEI 38 is selected for further analysis of its perfor-  
 692 mance throughout the entire BS process. As shown in Fig. 12,  
 693 GEI 38 minimizes its load and HVAC consumption while  
 694 maximizing BESS discharge and PV generation until it is  
 695 restored at 10:00. Once restored, its power consumption and  
 696 generation follow the utility’s dispatch signal. Throughout  
 697 the process, the indoor temperature remains within the accept-  
 698 able comfort range, demonstrating effective coordination of energy  
 699 resources.

664  
665

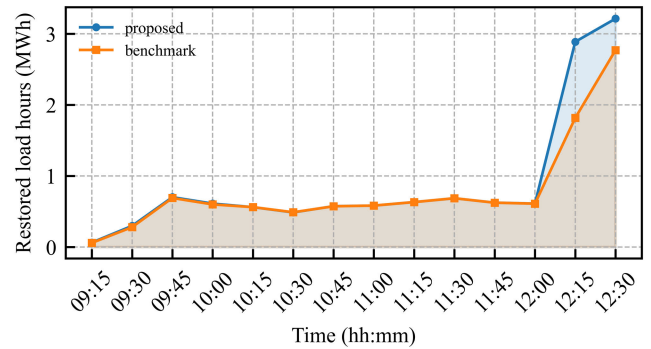
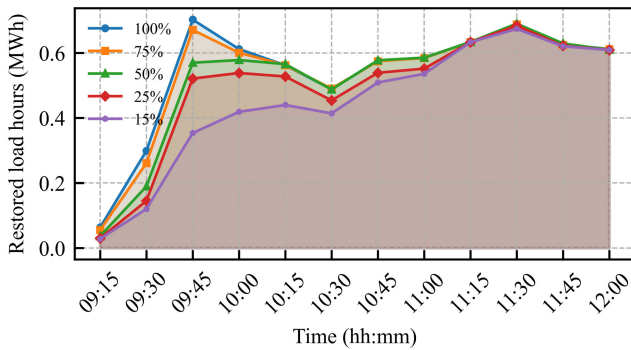
666  
667  
668  
669  
670  
671  
672  
673  
674  
675  
676  
677  
678  
679

680  
681  
682  
683  
684  
685  
686  
687  
688  
689  
690  
691  
692  
693  
694  
695  
696  
697  
698  
699  
700  
701



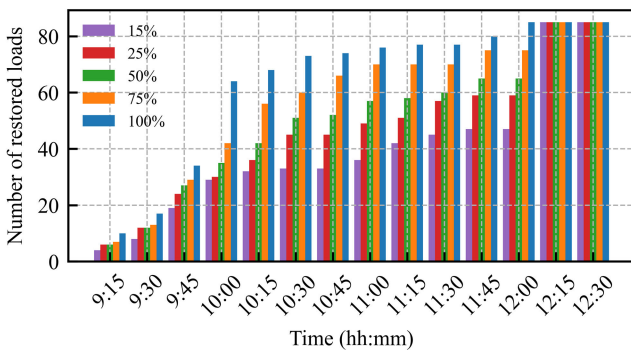
702 Fig. 12. Operation of house 38 with GEI during the restoration period.

711 Fig. 15. Frequency responses of GFMI in the benchmark method.



703 Fig. 13. Comparison in terms of restored load hours.

712 Fig. 16. Comparison of restoration performance with the benchmark method.



704 Fig. 14. Comparison in terms of number of houses being restored.

705 *C. Comparison With Different Flexible Load Level*

706 To demonstrate the advantages of GEI during BS and  
 707 load restoration, several simulations are conducted with vary-  
 708 ing levels of GEI penetration. In this study, residential  
 709 houses are progressively equipped with GEI devices, rang-  
 710 ing from 15% to 100%, and the proposed framework is

713 evaluated for each case. The final simulation results are  
 714 compared in terms of restored load-hours and the num-  
 715 ber of restored loads, as shown in Fig. 13 and Fig. 14,  
 716 respectively.

717 With only 15% GEI penetration, the total restored load-  
 718 hours amount to 5.36 MWh, whereas at 100% penetration, it  
 719 increases to 6.44 MWh. As shown in Fig. 14, the number of  
 720 houses restored is consistently higher with 100% GEI at each  
 721 time step prior to TG synchronization, which occurs at 12:00.  
 722 For other penetration levels, significant number of houses  
 723 are restored after TG synchronization. These results clearly  
 724 indicate that higher GEI penetration not only accelerates  
 725 the restoration process but also enables the system to serve  
 726 a significant portion of energy demand during the outage  
 727 period.

728 *D. Comparison With Benchmark Method*

729 To further demonstrate the superiority of the proposed  
 730 method, we conduct a comparative analysis against the bench-  
 731 mark method presented in [10]. In the benchmark approach,

rule-based synchronization is applied during BS. Before TG recovery, only the ESWs are optimized, while the SSWs are executed in a predefined sequence once the TG becomes available. The frequency response of the GFM-based BESS under the benchmark method is illustrated in Fig. 15. At the onset of BS, both GFMs operate at 60 Hz. Subsequently, the two GFMs operate at distinct frequencies until synchronization with the TG occurs, one at 12:00 and the other at 12:15. Moreover, the RoCoF and the frequency nadir for both GFMs remain within secure operational limits.

The load restoration performance for the case where the TG returns at 11:45 is presented in Fig. 16. It can be observed that optimizing both ESWs and SSWs not only expedites load restoration but also increases customer-hours served. Overall, the proposed method exhibits a noticeable advantage over the benchmark in restoration performance, particularly for longer-duration outages.

## VI. CONCLUSION

This paper proposes a predictive framework for a bottom-up black start strategy that leverages dynamic coordination between GEI and the utility to accelerate load restoration in the DS. The proposed coordination scheme requires GEI devices to communicate their flexibility ranges and the utility to provide dispatch signals, without the need to share detailed asset information between the two parties. A predictive model for GEI is developed to accurately quantify multi-period flexibility ranges and to track the utility's dispatch signals. Furthermore, the proposed BS strategy incorporates frequency security constraints, energization conditions, and synchronization requirements, enabling the dynamic formation of multiple microgrids and their integration to facilitate mutual sharing of power and energy capacity. The effectiveness of the proposed method is validated on a modified IEEE 123-bus test system, configured with two GFMs and evaluated under varying levels of GEI penetration. The results demonstrate that the approach significantly enhances system resilience by enabling rapid load restoration and maximizing the utilization of behind-the-meter DERs with GEI.

This work adopts deterministic forecasts for both load and PV generation. Consequently, uncertainty is not explicitly modeled, and the potential errors in the estimated flexibility boundaries under uncertain conditions could not be formally quantified. In future work, we aim to extend the framework to stochastic formulation that incorporates robust flexibility boundaries.

## REFERENCES

- [1] Z. Wang and J. Wang, "Self-healing resilient distribution systems based on sectionalization into microgrids," *IEEE Trans. Power Syst.*, vol. 30, no. 6, pp. 3139–3149, Nov. 2015.
- [2] Z. Wang, B. Chen, J. Wang, and C. Chen, "Networked microgrids for self-healing power systems," *IEEE Trans. Smart Grid*, vol. 7, no. 1, pp. 310–319, Jan. 2016.
- [3] W. Sun, C.-C. Liu, and L. Zhang, "Optimal generator start-up strategy for bulk power system restoration," *IEEE Trans. Power Syst.*, vol. 26, no. 3, pp. 1357–1366, Aug. 2011.
- [4] G. Patsakis, D. Rajan, I. Aravena, J. Rios, and S. Oren, "Optimal black start allocation for power system restoration," *IEEE Trans. Power Syst.*, vol. 33, no. 6, pp. 6766–6776, Nov. 2018.
- [5] Q. Wang, X. Zhang, Y. Xu, Z. Yi, and D. Xu, "Planning of stationary-mobile integrated battery energy storage systems under severe convective weather," *IEEE Trans. Sustain. Energy*, vol. 16, no. 2, pp. 1253–1268, Apr. 2025.
- [6] M. Braun et al., "The future of power system restoration: Using distributed energy resources as a force to get back online," *IEEE Power Energy Mag.*, vol. 16, no. 6, pp. 30–41, Nov. 2018.
- [7] W. Liu and F. Ding, "Hierarchical distribution system adaptive restoration with diverse distributed energy resources," *IEEE Trans. Sustain. Energy*, vol. 12, no. 2, pp. 1347–1359, Apr. 2021.
- [8] Y. Wang et al., "Coordinating multiple sources for service restoration to enhance resilience of distribution systems," *IEEE Trans. Smart Grid*, vol. 10, no. 5, pp. 5781–5793, Sep. 2019.
- [9] F. Sadeque and B. Mirafzal, "Frequency restoration of grid-forming inverters in pulse load and plug-in events," *IEEE J. Emerg. Sel. Topics Ind. Electron.*, vol. 4, no. 2, pp. 580–588, Apr. 2023.
- [10] S. Maharjan, C. Bai, H. Wang, Y. Yao, F. Ding, and Z. Wang, "Distribution system blackstart and restoration using DERs and dynamically formed microgrids," *IEEE Trans. Smart Grid*, vol. 16, no. 3, pp. 2100–2114, May 2025.
- [11] S. Maharjan, A. Trivedi, and D. Srinivasan, "Rules-integrated model predictive control of office space for optimal electricity prosumption," *Sustain. Energy, Grids Netw.*, vol. 33, Mar. 2023, Art. no. 100981.
- [12] A. Arif, S. Ma, Z. Wang, J. Wang, S. M. Ryan, and C. Chen, "Optimizing service restoration in distribution systems with uncertain repair time and demand," *IEEE Trans. Power Syst.*, vol. 33, no. 6, pp. 6828–6838, Nov. 2018.
- [13] B. Chen, Z. Ye, C. Chen, and J. Wang, "Toward a MILP modeling framework for distribution system restoration," *IEEE Trans. Power Syst.*, vol. 34, no. 3, pp. 1749–1760, May 2019.
- [14] A. Arif, B. Cui, and Z. Wang, "Switching device-cognizant sequential distribution system restoration," *IEEE Trans. Power Syst.*, vol. 37, no. 1, pp. 317–329, Jan. 2022.
- [15] J. C. Bedoya, Y. Wang, and C.-C. Liu, "Distribution system resilience under asynchronous information using deep reinforcement learning," *IEEE Trans. Power Syst.*, vol. 36, no. 5, pp. 4235–4245, Sep. 2021.
- [16] Y. Du and D. Wu, "Deep reinforcement learning from demonstrations to assist service restoration in islanded microgrids," *IEEE Trans. Sustain. Energy*, vol. 13, no. 2, pp. 1062–1072, Apr. 2022.
- [17] O. Bassegy, K. L. Butler-Purry, and B. Chen, "Dynamic modeling of sequential service restoration in islanded single master microgrids," *IEEE Trans. Power Syst.*, vol. 35, no. 1, pp. 202–214, Jan. 2020.
- [18] L. Che and M. Shahidehpour, "Adaptive formation of microgrids with mobile emergency resources for critical service restoration in extreme conditions," *IEEE Trans. Power Syst.*, vol. 34, no. 1, pp. 742–753, Jan. 2019.
- [19] Q. Zhang, Z. Ma, Y. Zhu, and Z. Wang, "A two-level simulation-assisted sequential distribution system restoration model with frequency dynamics constraints," *IEEE Trans. Smart Grid*, vol. 12, no. 5, pp. 3835–3846, Sep. 2021.
- [20] M. Song, R. R. Nejad, and W. Sun, "Robust distribution system load restoration with time-dependent cold load pickup," *IEEE Trans. Power Syst.*, vol. 36, no. 4, pp. 3204–3215, Jul. 2021.
- [21] A. F. Taha, N. Gatsis, B. Dong, A. Pipri, and Z. Li, "Buildings-to-grid integration framework," *IEEE Trans. Smart Grid*, vol. 10, no. 2, pp. 1237–1249, Mar. 2019.
- [22] X. Jin, X. Wang, H. Jia, Y. Mu, Q.-W. Wu, and W. Wei, "Peer-to-peer multi-energy trading among heterogeneous building prosumers via asynchronous distributed algorithm," *IEEE Trans. Smart Grid*, vol. 16, no. 2, pp. 1590–1603, Mar. 2025.
- [23] R. Cheng, Z. Wang, Y. Guo, and Q. Zhang, "Online voltage control for unbalanced distribution networks using projected Newton method," *IEEE Trans. Power Syst.*, vol. 37, no. 6, pp. 4747–4760, Nov. 2022.

857  
858  
859  
860  
861  
862  
863  
864  
865  
866  
867

**Junyuan Zheng** (Graduate Student Member, IEEE) received the B.S. degree in electrical engineering and automation and the M.S. degree in control science and engineering from Northeast Forestry University, Harbin, China, in 2021 and 2024, respectively. He is currently pursuing the Ph.D. degree with the Department of Electrical and Computer Engineering, Iowa State University, Ames, IA, USA. His current research interests include power system restoration, and control and optimization of distribution systems.

868  
869  
870  
871  
872  
873  
874  
875  
876  
877  
878  
879  
880

**Salish Maharjan** (Senior Member, IEEE) received the Ph.D. degree in electrical and computer engineering from the National University of Singapore, Singapore, in 2020. He was a Visiting Student with Massachusetts Institute of Technology, Cambridge, MA, USA, in 2014. He is currently a Research Assistant Professor with the Department of Electrical and Computer Engineering, Iowa State University, Ames, IA, USA. His research interests include distribution system modeling, stability analysis, optimization and control for techno-economic operation, and resilience enhancement. He was a recipient of the Best Paper Award in 2023 and 2025 IEEE Power and Energy General Meeting.



**Zhaoyu Wang** (Fellow, IEEE) received the B.S. and M.S. degrees in electrical engineering from Shanghai Jiao Tong University, and the M.S. and Ph.D. degrees in electrical and computer engineering from Georgia Institute of Technology. Since 2015, he has been an Assistant, an Associate, and a Full Professor with Iowa State University. He is the lead Principal Investigator for over \$24M projects funded by the National Science Foundation, the Department of Energy, the National Laboratories, PSERC, and Iowa Economic Development Authority. His research interests include optimization and data analytics in power distribution systems and microgrids. He was a recipient of the National Science Foundation CAREER Award, the IEEE Power and Energy Society (PES) Outstanding Young Engineer Award, the ISU Award for Mid-Career Achievement in Research, the Northrop Grumman Endowment, the ISU College of Engineering's Early Achievement in Research Award, and the Harpole-Pentair Young Faculty Award Endowment. He is an IEEE PES Distinguished Lecturer. He is the Secretary and the Technical Committee Program Chair (TCPC) of IEEE Power System Operation, Planning, and Economics (PSOPE) Committee, the Chair of IEEE Distribution System Operation and Planning Subcommittee, the Secretary of IEEE Task Force on IEEE P3102 Standard for Conservation Voltage Reduction (CVR) Data Collection and Management Procedures, and the Chair of IEEE Task Force on Advances in Natural Disaster Mitigation Methods. He was an Associate Editor of IEEE TRANSACTIONS ON POWER SYSTEMS, IEEE TRANSACTIONS ON SMART GRID, and IEEE OPEN ACCESS JOURNAL OF POWER AND ENERGY. He is an Associate Editor of IEEE TRANSACTIONS ON SUSTAINABLE ENERGY, IEEE POWER ENGINEERING LETTERS, and *IET Smart Grid*.

881  
882  
883  
884  
885  
886  
887  
888  
889  
890  
891  
892  
893  
894  
895  
896  
897  
898  
899  
900  
901  
902  
903  
904  
905  
906  
907  
908  
909